Biophysical Journal
Article

Biophysical Society

Enhancing Irreversible Electroporation by Manipulating Cellular Biophysics with a Molecular Adjuvant

Jill W. Ivey,[1] Eduardo L. Latouche,[2] Megan L. Richards,[1] Glenn J. Lesser,[3] Waldemar Debinski,[3] Rafael V. Davalos,[2,3] and Scott S. Verbridge[1,3,*]

[1]Laboratory for Integrative Tumor Ecology and [2]Bioelectromechanical Systems Laboratory, Department of Biomedical Engineering and Mechanics, Virginia Tech-Wake Forest University School of Biomedical Engineering & Sciences, Blacksburg, Virginia; and [3]Brain Tumor Center of Excellence, Comprehensive Cancer Center, Wake Forest Baptist Medical Center, Winston-Salem, North Carolina

ABSTRACT Pulsed electric fields applied to cells have been used as an invaluable research tool to enhance delivery of genes or other intracellular cargo, as well as for tumor treatment via electrochemotherapy or tissue ablation. These processes involve the buildup of charge across the cell membrane, with subsequent alteration of transmembrane potential that is a function of cell biophysics and geometry. For traditional electroporation parameters, larger cells experience a greater degree of membrane potential alteration. However, we have recently demonstrated that the nuclear/cytoplasm ratio (NCR), rather than cell size, is a key predictor of response for cells treated with high-frequency irreversible electroporation (IRE). In this study, we leverage a targeted molecular therapy, ephrinA1, known to markedly collapse the cytoplasm of cells expressing the EphA2 receptor, to investigate how biophysical cellular changes resulting from NCR manipulation affect the response to IRE at varying frequencies. We present evidence that the increase in the NCR mitigates the cell death response to conventional electroporation pulsed-electric fields ($\sim$100 μs), consistent with the previously noted size dependence. However, this same molecular treatment enhanced the cell death response to high-frequency electric fields ($\sim$1 μs). This finding demonstrates the importance of considering cellular biophysics and frequency-dependent effects in developing electroporation protocols, and our approach provides, to our knowledge, a novel and direct experimental methodology to quantify the relationship between cell morphology, pulse frequency, and electroporation response. Finally, this novel, to our knowledge, combinatorial approach may provide a paradigm to enhance in vivo tumor ablation through a molecular manipulation of cellular morphology before IRE application.

INTRODUCTION

Electroporation describes the phenomenon of using an electric field to permeabilize the membrane of a cell by inducing a transmembrane potential large enough to induce a disruption in the lipid bilayer. Once the transmembrane potential reaches a critical value of $\sim$250 mV, transient nanoscale pores form in the membrane, allowing the passage of otherwise excluded molecules through the membrane barrier (1). This reversible electroporation technique has been used for gene transfection, gene therapy, and cancer electrochemotherapy (ECT) (2,3). When the transmembrane potential reaches another critical value of $\sim$1 V, the cell cannot recover from the pore formation and dies due to loss of homeostasis (4). This method of cell ablation, termed irreversible electroporation (IRE), has been used for the treatment of a variety of cancers, including prostate, pancreas, and liver cancers (5–8).

IRE as a cancer treatment method has many advantages over other approaches. The non-thermal nature of the treatment allows for the sparing of extracellular matrix and vital structures such as blood vessels while producing a more uniform ablation due to the lack of a heat-sink effect (9). IRE ablation methods are able to achieve cell-scale ($\sim$50 μm) resolution between ablated and non-ablated zones (9,10), allowing for ablation regions to be predicted by pre-treatment planning (11). In addition, real-time monitoring by imaging and impedance measurements can be done to ensure proper electrode placement and complete ablation (12,13). Although the benefits of this treatment modality have underpinned its successful use for a variety of cancers, invasive cancers such as glioblastoma (GBM) still present challenges. IRE methods do not allow for the treatment of diffuse cells outside the tumor margin without ablation of healthy tissue, a situation especially problematic in the

Submitted April 13, 2017, and accepted for publication June 9, 2017.

*Correspondence: sverb@vt.edu

Editor: Jennifer Curtis.

http://dx.doi.org/10.1016/j.bpj.2017.06.014

brain. To address these challenges and improve selectivity outside the tumor margin, investigators have begun studying combination therapies such as IRE used with ECT (14).

To increase the selective capabilities of IRE treatment, here we investigate a new combinatorial treatment concept, combining electroporation with a molecular therapy that we hypothesized would act in a synergistic manner to the physical treatment. Our previous research efforts have identified the receptor EphA2 as a promising target for selective molecular treatment for GBM (15). EphA2, a member of the largest class of receptor tyrosine kinases, is overexpressed in GBM tissue in a predominantly inactive state (15), as its preferred ligand ephrinA1 (eA1) is present at diminished levels compared to the level in normal brain tissue (16,17). Our research efforts have shown that exogenous soluble eA1 is a functional ligand for EphA2 (18), and progress has been made in creating ephrin-based therapeutic agents through conjugation of a bacterial toxic protein to soluble eA1 that selectively targets GBM cells (19). From this work developing an ephrin-based molecular targeted therapy, we noted a selective morphology change in GBM cells upon exposure to eA1. This physical response, characterized by a rounding of the cell and a shrinking of the cell cytoplasm (18,20,21), formed the basis of the here presented investigation into a combinatorial treatment with IRE therapies.

In considering IRE, the physical attributes of a cell are important, as electroporation is dependent on both cell size and morphology. The effect of cell size on electroporation has been demonstrated for a variety of pulse widths ranging from a few microseconds (22) to hundreds of milliseconds (23). The steady-state scenario is valid for the understanding of electroporation phenomenon involved in typical IRE protocols used in the treatment of cancer. These protocols involve the application of around 90 pulses of 50–100 μs duration delivered through electrodes inserted into the tissue (5,24). We have shown that by reducing the duration of the electric field pulses to be shorter than the charging time of the cell membrane, the field can penetrate the cell interior, and the dependence of electroporation on cell size is reduced (25,26). This shorter pulse technique, termed high-frequency IRE (H-FIRE), which uses trains of ≤ 2 μs duration bipolar pulses, exposes inner organelles to large electric fields. H-FIRE acts on cells in such a way that nuclear size becomes a more important predictor of cell death than cell size, with a lower electric field needed to kill cells with a higher nuclear/cytoplasm ratio (NCR) (25).

Despite some efforts to predict the transmembrane potential (TMP) of cells exposed to pulsed electric fields (PEFs) on the order of a few microseconds, no mathematical models for cells of a high NCR have been developed (27,28). In this study, we look further into the impact of cell size and morphology on the electroporation phenomenon at short pulse lengths, where the steady-state electroporation equation breaks down and frequency is known to play an important role in predicting induced TMP. Equipped with the finding that the NCR is an important predictor of electroporation using H-FIRE pulse lengths, we investigated the NCR effect on H-FIRE ablation by combining H-FIRE therapy with a molecular intervention using eA1 to increase NCR.

The overabundance of EphA2 receptor and the diminished presence of eA1 in GBM tissue open up this receptor-ligand interaction as a unique method for selectively tuning cell morphology to isolate the NCR effect on H-FIRE. These biological cell manipulations allow us to discover electroporation behaviors in the pulse space where traditional analytical model predictions do not apply. Additionally, this work highlights a novel correlation—an increase in electroporation efficacy due to decreasing cell size—thereby highlighting the complexities ignored by the Schwan equation in describing cell response to electric fields with short pulses.

MATERIALS AND METHODS

Cell culture

U-87 MG human GBM cells (ATCC, Manassas, VA) were cultured in Dulbecco's modified Eagle's medium (DMEM) containing 10% fetal bovine serum (FBS) and 1% penicillin/streptomycin (PS). Normal human astrocyte (NHA) cells (Lonza, Basel, Switzerland) were cultured in astrocyte growth media (Lonza). U-251 MG human GBM cells (ATCC) cells were grown in DMEM containing 10% FBS, 1% PS, and 0.1 mM non-essential amino acid. DBTRG human glioblastoma cells (ATCC) were cultured in RPMI medium containing 10% FBS, 2 mM L-glutamine, 1% PS, and 0.1 mM non-essential amino acids. All cells were grown in culture at 37°C in 5% CO2 in a humidified incubator. Cells were seeded in hydrogels at a density of 1×10^6 cells/mL. The hydrogels were submerged in appropriate growth media for the cell type at 37°C in 5% CO_2 in a humidified incubator, and cell viability was maintained within hydrogels for up to 7 days.

Construction of collagen scaffolds

Stocks of type I collagen were prepared by dissolving rat tail tendon in acetic acid, followed by freezing and lyophilization, as described previously (29). Stock solution concentrations of collagen were created at a density of 10 mg/mL. Scaffolds with a final concentration of 5 mg/mL were made from concentrated collagen stocks to create collagen gels of 0.5% (w/w). Neutralized collagen solutions were created by mixing acid-dissolved collagen with 10× DMEM (10% of total collagen solution volume) and sufficient volumes of 1 N NaOH until a pH in the range 7.0–7.4 was achieved. The neutralized collagen was mixed with cells suspended in DMEM or NHA media to achieve a cell density of 1×10^6 cells/mL in the final collagen mixture. Solutions were mixed carefully with a sterilized spatula to ensure homogenous distribution throughout the gel without damaging cells. Collagen solutions were then dispensed into a polydimethylsiloxane (PDMS) mold with a cut-out of 10 mm diameter and 1 mm depth and molded flat to ensure consistent scaffold geometry. Our previous mathematical modeling and experiments on oxygen (O_2) consumption rates by tumor cells (29) confirms that at this cell density and scaffold thickness, O_2 concentration is uniform throughout the scaffold depth. Collagen was allowed to polymerize at 37°C and 5% CO_2 for 30 min.

Treatment with eA1

Cells seeded in collagen hydrogels were cultured for 24 h after seeding to allow for cells to engage the collagen and achieve a physiologically relevant morphology. After 24 h, hydrogels in the eA1-treated condition were cultured in serum-free cell culture media with 1 μg/mL eA1-FC (R&D Systems) added to the media for 12 h before electroporation treatment or fixation for immunofluorescence staining. Control cells were cultured in hydrogels submerged in serum-free culture media without the added eA1-FC for 12 h before use in experiments. The 12 h time point was chosen because a full morphological change of the cells within the hydrogels was seen by 12 h and no further changes were observed at longer exposure times. No difference was seen in viability between hydrogels cultured in eA1-FC-conditioned media and control media before exposure to electroporation therapy (Fig. S1).

Fluorescent staining

U-87, U251, DBTRG, and NHA cells were individually seeded in hydrogels described previously. After culturing the cells for 24 h for engagement with the matrix and then for an additional 12 h after treatment, the hydrogels were fixed using 4% formalin and blocked and permeabilized using 40 mg/mL bovine serum albumin (BSA) and 0.05% Triton-X. Cellular F-actin was stained with Alexa Fluor 568 phalloidin (Life Technologies, Carlsbad, CA), whereas cell nuclei were stained with diaminophenylindole (DAPI; Sigma-Aldrich, St. Louis, MO). Cells were visualized using a Zeiss LSM880 (Carl Zeiss Microscopy, Thornwood, NY) laser scanning confocal microscope.

Determination of the NCR

Untreated hydrogels seeded at the same cell density and collagen conditions as treated hydrogels were fixed and fluorescently stained to determine overall cell area and nuclear area for cells in the control condition and in the ephA1-treated condition. Measurements were made on at least four cells per hydrogel, and at least five hydrogels were analyzed for each condition so at least 20 cells were used to determine average NCR for each cell type in each condition. Image analysis was done in Image J (National Institutes of Health, Bethesda, MD). Z-stack images were converted to 2D projection images and cell measurements were made from these projections. NCR was calculated from the measured cell area (A_C) and nuclear area (A_N) as follows:

$$\mathrm{NCR} = \frac{A_N}{A_C - A_N}. \quad (1)$$

Finite-element analysis in hydrogels

Finite-element models using COMSOL Multiphysics (Version 4.3; COMSOL, Palo Alto, CA) were used to solve the Laplace equation to find the electric field distribution within the hydrogels for each different voltage used. The electric field distribution within the hydrogel was found by solving the Laplace equation,

$$\nabla^2 \phi = 0, \quad (2)$$

where ϕ is the electrical potential. The boundaries of one electrode were set to the applied voltage ($\phi = V_{\mathrm{applied}}$) and the boundaries of the second electrode were set to ground ($\phi = 0$) while the initial voltage (V_0) for all subdomains was set to 0 V. All other external boundaries were set to electrical insulation ($-\boldsymbol{n}\cdot\boldsymbol{J} = 0$). The mesh was refined until error between successive refinements was <1%. The final mesh contained 47,438 elements, and solutions were found in ~3 min on a Pentium i3 processor.

Finite-element analysis of individual cells based on NCR

The electrodynamic solutions of interest were reached by modeling a spherical cell membrane and nuclear envelope and solving a finite-element model with an impedance boundary condition scheme as previously described (25,30). The models used to investigate the membrane response to different pulse parameters changed the NCR based on representative cell geometries determined based on average measurements made in ImageJ image analysis software (National Institutes of Health) from confocal microscopy images. To better understand the effect of high-frequency components of H-FIRE on individual cells, a frequency-dependent module was used to mimic the increase in frequency for different H-FIRE pulse lengths and IRE-type pulses. The geometry and physical properties of the cell can be found in Table S2.

Simulations were solved in the frequency domain using an electric-currents module, which has been previously shown to correlate well for spherical cells exposed to rectangular pulses in the order of 1–2 μs (28). To account for the impedance posed by the membranes of the cell and nucleus, their boundaries were assigned impedance properties found in the literature (Table S2).

Electroporation techniques

Pulsed electroporation experiments were performed in collagen hydrogels with constant electrical properties. High-frequency pulses were delivered using a custom-built pulse generation system (INSPIRE 2.0; VoltMed, Blacksburg, VA). Pulses were delivered through custom-built electrodes composed of two solid stainless steel cylinders with diameters of 0.87 mm separated by 3.3 mm edge to edge, with spacing and geometry maintained by a three-dimensional printed electrode holder. In the H-FIRE pulsing protocol, treatments were performed delivering 50 bursts of 1 μs bipolar pulses. A burst consisted of 100 × 1 μs pulses of alternating polarity with a 5 μs inter-pulse delay delivered with a repetition rate of one burst per second. Voltage output was set to 700 V to achieve measurable lesions within the hydrogel geometry. Conventional IRE pulses were delivered using an ECM 830 pulse generator (Harvard Apparatus, Holliston, MA) through the same custom-built electrodes. These treatments consisted of 50 square pulses of 100 μs pulse width with a repetition rate of one pulse per second. IRE voltage output was set to 350 V to achieve measurable lesions within the hydrogel geometry.

Determination of lethal threshold in hydrogels

The thresholds for cell death were determined by first performing a live-dead stain on the hydrogels 24 h after delivering treatment. Live cells were stained with calcein AM (Biotium, Hayward, CA) and fluoresced as green, whereas dead cells were stained with ethidium homodimer III (Biotium) and fluoresced as red. The size of the red-stained dead region was measured using ImageJ image analysis software. Geometric measurements of the ablation zones were mapped to a finite-element model to calculate the electric field during treatments of the scaffolds. The electric field magnitude at the edge of the live and dead regions was considered the electric field threshold for cell death for the given cell type. Each individual hydrogel exposed to either H-FIRE therapy or H-FIRE-with-eA1 therapy measured to determine the lethal electric field for the cell type was considered an independent sample representing the response of ~125,000 cells. For each condition, hydrogels were pulsed in at least three different independent experiments on different days.

Power spectral analysis

A power spectral analysis was conducted by running a fast Fourier transform on the experimental H-FIRE pulses. The power spectral analysis

was used to determine the dominant frequencies a cell is exposed to upon treatment, as demonstrated elsewhere as a tool for understanding bipolar pulses (31).

Statistical analysis

Statistical significance was determined by a two-tailed *t*-test performed in Prism Statistical Software (Version 6; Graphpad, La Jolla, CA). A 95% confidence interval was used, with significance defined as $p < 0.05$. All numerical results are reported as the mean ± SD of all experimental measurements. No outliers were excluded.

Data availability

The data sets generated and analyzed during this study are available from the corresponding author on reasonable request.

RESULTS

EphA2 activation by eA1 induces a targeted morphology change in malignant cells

To investigate the dynamics of eA1-induced morphology changes, we cultured malignant GBM and normal brain cells in three-dimensional hydrogels and exposed them to eA1. EphA2 activation by eA1 in malignant cell lines (U-87 MG, U-251 MG, and DBTRG) led to visible cell morphology changes characterized by cell rounding and a collapse of the cytoplasm (Fig. 1 *a*). Cell rounding was visible after 6 h of culture in media containing eA1 (1 μg/mL), with the full morphological change accomplished by 12 h. In NHA cells, no morphological change was observed at any time point out to 48 h when culturing hydrogels in eA1 media. For the malignant cell lines, the cytoplasm collapse upon EphA2 activation resulted in a significant change in the NCR of the cells (Fig. 1 *b*). NHA cells showed no significant change in NCR under these treatment conditions. No morphology change was observed in control tumor cells cultured in media without eA1 present.

Extent of electroporation for different cell morphologies is dependent on frequency of the electric field

Finite-element modeling was used to predict the induced TMP for a variety of cell morphologies as a function of the frequency of a steady-state, alternating-current electric field. Characteristic morphologies determined from experimental culture of glioma cells, normal astrocytes, and glioma cells treated with eA1 were used. At lower frequencies, characteristic of IRE pulse waveforms, larger cells experience a greater induced transmembrane potential compared with a glioma cell that shrinks in volume due to treatment with eA1. At a frequency of ~10 kHz, the enlarged nucleus of the glioma cell causes it to experience a greater transmembrane potential

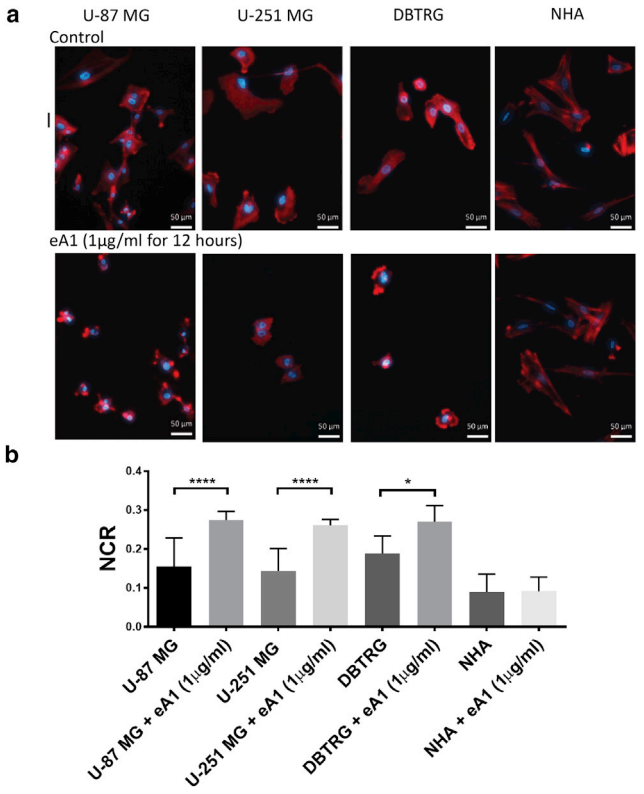

FIGURE 1 Treatment with soluble eA1 causes glioma morphology change while not altering NCR for astrocytes. (*a*) Malignant cells stained with DAPI (*blue*) and phalloidin (*red*) cultured in media with 1 μg/mL eA1 for 12 h exhibit cell rounding and a collapse of the cytoplasm around the nucleus, whereas healthy cell morphology remains unchanged upon exposure to eA1. Scale bars, 50 μm. (*b*) eA1-induced morphology change results in a quantitative increase in NCR for malignant cells, whereas the NCR remains unchanged for normal astrocytes. $n = 20$; $^{****}p \leq 0.0001$, $^{*}p = 0.027$. To see this figure in color, go online.

than an astrocyte of the same size but with a smaller nucleus. This trend continued throughout higher frequencies of electric field, suggesting that fields of frequency >10 kHz can be used to accomplish greater electroporation in cells with a larger nucleus than in cells with a smaller nucleus. At an electric field frequency of ~100 kHz, the smaller cell experiences a larger induced transmembrane potential than the larger cells, suggesting a greater extent of electroporation in smaller cells with an enlarged nucleus than in larger cells.

As the duration of the applied pulse is decreased, a greater proportion of the power is concentrated in higher-frequency signal content. The experimental pulse train of 1 μs bipolar pulses with a 5 μs delay between pulses (Fig. 2 *a*) delivers the majority of its power between 100 kHz and 1000 kHz (Fig. 2 *b*). Interestingly, these frequencies correspond to the frequencies predicted to allow for a crossover in TMP for the eA1-induced cell morphologies when exposed to an alternating-current signal (Fig. 2 *c*).

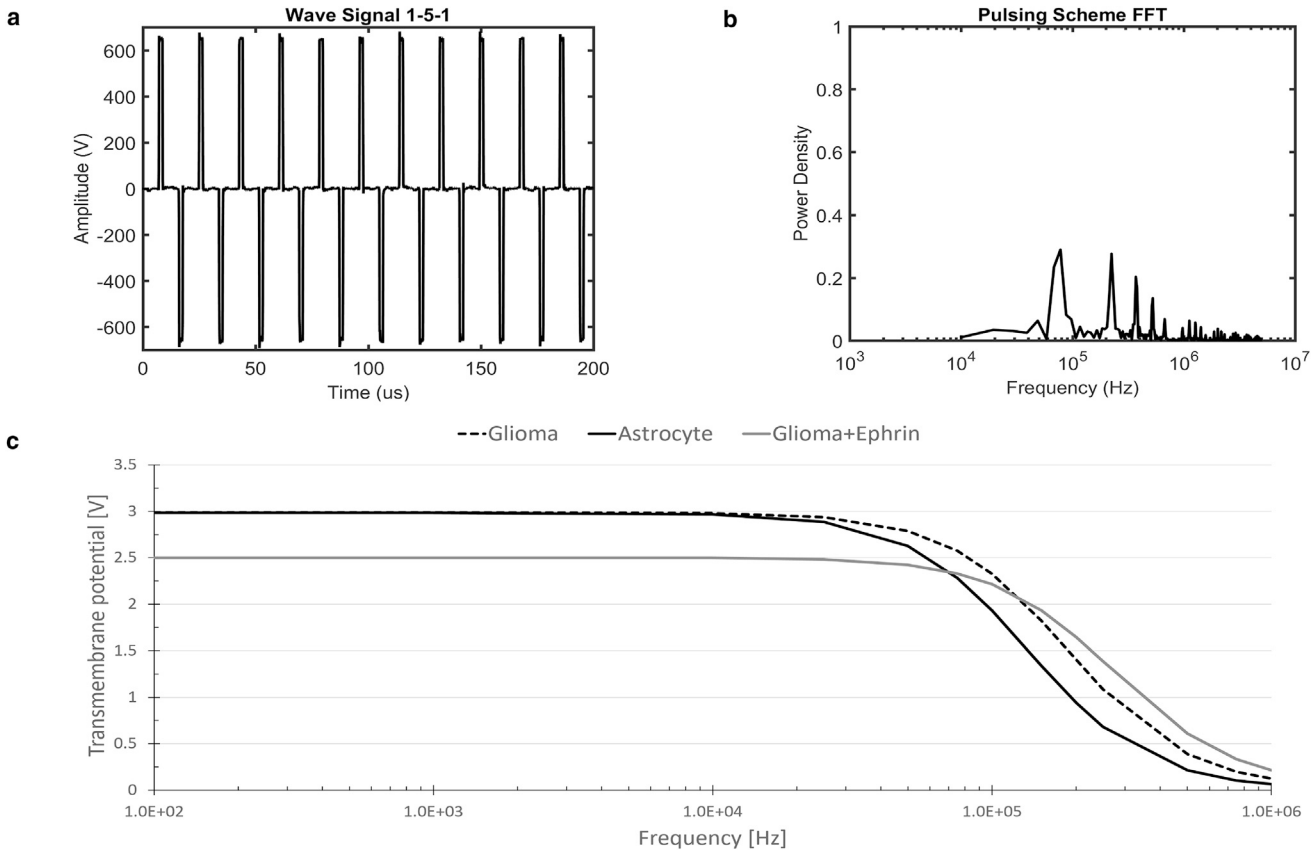

FIGURE 2 (*a*) Experimental pulse waveform applied to hydrogels. A bipolar waveform of 1 μs pulses separated by a 5 μs delay was used to accomplish electroporation in a hydrogel platform. (*b*) Power-spectrum analysis of an experimental pulse train. The amplitude frequency distribution found by fast Fourier transform of experimental pulse trains shows that the pulse train of 1 μs bipolar pulses separated by a 5 μs delay delivers the majority of its power at frequencies around 100 kHz. (*c*) Single-cell steady-state response to an electric field of 1000V/cm applied as an alternating-current signal. As expected, larger cells (U87 and astrocyte) present larger TMPs at lower frequencies. However, cells of higher NCR will have larger TMPs at higher frequencies (>100 kHz).

Morphology change impacts lethal thresholds for electroporation of malignant cells

To determine whether the increase in the NCR in malignant cells led to a change in the H-FIRE threshold as predicted by finite-element modeling, eA1-treated hydrogels were exposed to a regimen of H-FIRE treatment and compared with control hydrogels. Malignant hydrogels treated with eA1 had significantly larger lesions than control hydrogels, whereas non-malignant hydrogels had no significant difference between conditions (Fig. 3 *a*). The increase in NCR for malignant cells corresponded to a smaller lethal threshold for H-FIRE, whereas the lethal threshold did not change for non-malignant cells (Fig. 3 *b*). For U87 cells, under normal conditions, the lethal threshold is 603 $\pm$ 65 V/cm (n = 8), whereas under treatment with eA1, the lethal threshold is 446 $\pm$ 55 V/cm (n = 8). For U-251 cells, under normal conditions, the lethal threshold is 662 $\pm$ 57 V/cm (n = 8), whereas under treatment with eA1, the lethal threshold is 415 $\pm$ 48 V/cm (n = 8). For DBTRG cells, under normal conditions, the lethal threshold is 712 $\pm$ 68 V/cm (n = 6), whereas under treatment with eA1, the lethal threshold is 532 $\pm$ 48 V/cm (n = 6). Lethal thresholds for non-malignant cell types remained unchanged. Control NHA cells are killed at a threshold of 1028 $\pm$ 47 V/cm (n = 6) and eA1-treated NHA cells have a lethal threshold of 1032 $\pm$ 82 V/cm (n = 6). For the most responsive cell type, U-251 cells, eA1 treatment resulted in a 37% decrease in the lethal threshold for H-FIRE therapy.

Similarly, eA1-treated hydrogels were exposed to traditional IRE pulses of 100 μs pulse width to determine whether these lesions would change as a result of the eA1-induced morphology change in treated cells. In contrast to the trend seen using H-FIRE pulses, IRE lesions of eA1-treated U-251 cells are significantly smaller than control hydrogels of U-251 cells cultured in normal media (Fig. 4). U-251 cells cultured in normal media within the hydrogels had an IRE lethal threshold of 517 $\pm$ 45 V/cm (n = 6). U-251 cells cultured with media containing 1 μg/mL eA1 within the hydrogels had an IRE lethal threshold of 684 $\pm$ 44 V/cm (n = 6).

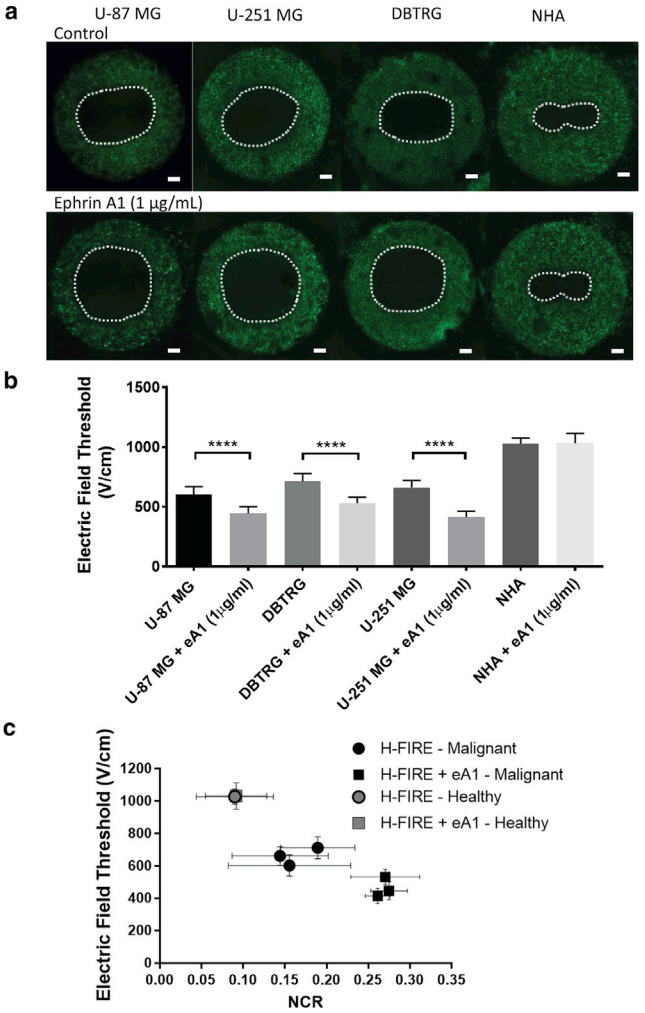

FIGURE 3 NCR change induced by eA1 enhances H-FIRE lesions in malignant cells. (*a*) H-FIRE lesion size for malignant glioma cells (U-87, U-251, and DBTRG) is increased relative to control cells when hydrogels are cultured with eA1 ligand. H-FIRE lesions in non-malignant astrocytes (NHAs) remain unchanged with eA1 exposure. Scale bars, 1 mm. (*b*) COMSOL modeling relating lesion size to lethal thresholds shows a significant decrease in H-FIRE lethal threshold for malignant cells when treated with eA1 prior to electroporation exposure. H-FIRE lethal threshold for non-malignant cells remains unchanged with eA1 exposure. (*c*) Summary of data shows a correlation between the average NCR of a given cell type in the hydrogel and the lethal electric-field threshold for that cell type in the hydrogel. Healthy astrocytes (*gray markers*) show no change with eA1 treatment, whereas malignant cells (*black markers*) show a decreased lethal electric-field threshold when treated with eA1 to induce an NCR increase. $****p \leq 0.0001$. To see this figure in color, go online.

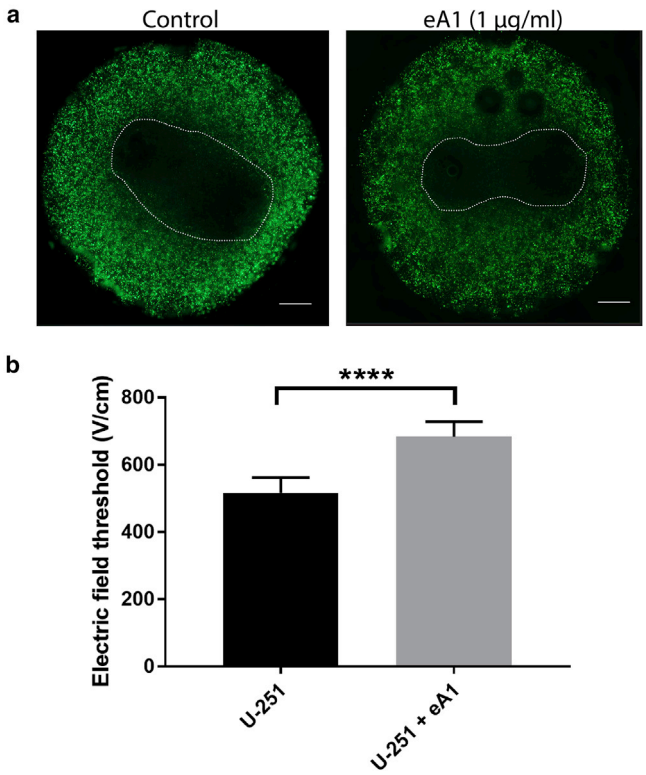

FIGURE 4 NCR change induced by eA1 results in smaller IRE lesions. (*a*) IRE lesion size for U-251 glioma cells is smaller compared to the control when hydrogels are cultured with eA1 ligand. Scale bars, 1 mm. (*b*) COMSOL modeling relating lesion size to lethal thresholds shows a significant increase in IRE lethal threshold for U-251 cells when treated with eA1 before electroporation exposure. $n = 6$; $****p \leq 0.0001$. To see this figure in color, go online.

eA1 treatment enhances malignant cell selectivity of H-FIRE

To demonstrate the enhanced selectivity of malignant cells possible with combination H-FIRE-and-eA1 treatment, we performed co-culture experiments. Hydrogels of NHAs and U-87 GBM cells were cultured in media containing eA1 and then exposed to a regime of H-FIRE pulses. Although selective killing of U87 cells and not NHA cells is achieved in the control condition, the region of U87 killing is significantly enlarged, whereas the NHA lesion remains the same for cells exposed to eA1 (Fig. 5).

DISCUSSION

We have demonstrated that the cell-size dependence for electroporation-induced cell death depends critically on frequency range. Each component of the cell—membrane, cytoplasm, and nuclear membrane—has a characteristic impedance that affects the TMP response to varying degrees depending on the cell morphology. As the capacitance of each part of the cell is dependent on the surface area, the change in morphology induced by eA1 treatment will produce changes in cell capacitance.

We hypothesize that the effect demonstrated here of high-frequency PEFs preferentially ablating cells of smaller volume but higher NCR may be due to changes in impedance of the cytoplasm. If part of the external field is able to bypass the cell membrane and interact with internal components of the cell, the impedances of the cytoplasm and nucleus become important factors. This effect, which can be exploited through treatment with eA1, will be magnified as

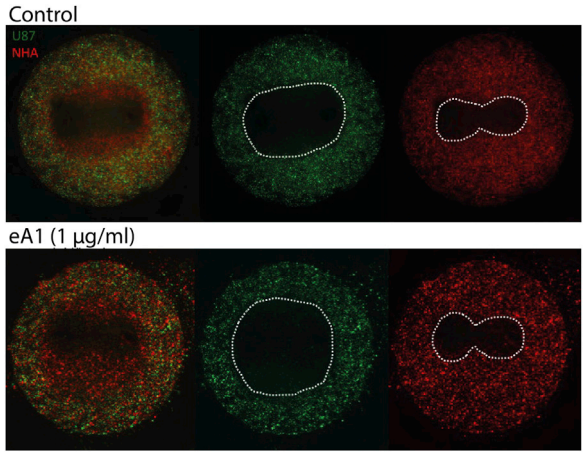

FIGURE 5 Treatment with eA1 enhances selectivity of H-FIRE for malignant cells in co-culture. The area of ablated malignant cells and live healthy cells is extended by treating co-culture hydrogels with eA1 before H-FIRE exposure. Scale bars, 1 mm. To see this figure in color, go online.

the volume of the cytoplasm is decreased. Therefore, for high-frequency pulses, the NCR of a cell becomes a significant variable in predicting electroporation response. This finding is significant for the understanding of electroporation theory, because it clearly illustrates that the relationship between cell size and electroporation is closely dependent on waveform frequency, which would impact electroporation protocols both for research and for therapeutic applications.

We have shown for the first time, to our knowledge, that molecular targeting with ensuing changes in GBM cell morphology may be used to enhance the selectivity of PEFs to induce tumor cell death. Selectivity, regulated by the NCR, opens up the possibility of enhanced targeted cancer therapy, as malignant cells are known to often have increased NCR compared to normal cells (32,33). Because the EphA2 receptor is overexpressed specifically on malignant cells in adulthood, the induced morphology change can be exploited in developing combinatorial targeted therapies using H-FIRE. The ability to selectively target cells with increased NCR is significant for the future of GBM treatment, because it may allow for the treatment of diffuse malignant cells that have invaded into normal brain tissue. By lowering the lethal threshold for malignant cells in the outermost regions of the tumor, where selectivity is most important, eA1 treatment may increase the margin of tumor that can safely be ablated with H-FIRE therapy regimes. Though many attempts have been made to use EphA2 as a direct therapeutic target (19,34), this work is the first, to our knowledge, that utilizes a resulting morphological change to enhance targeting by combination with a physical therapy in the form of PEFs. We furthermore note that short ($\sim$1 μs) pulses in particular are necessary to induce this synergistic tumor cell death response, as we have demonstrated that longer ($\sim$100 μs) IRE pulses of the sort most commonly used for clinical tumor ablation (5,7) become less effective in combination with sub-lethal eA1 treatment in our studies. Though this work represents early stages in the development of cell-selective electroporation techniques, the results presented here suggest the ability of such techniques to optimize parameters to further increase the selectivity, with the possibility of efficacy in an in vivo context. The performed power spectral analysis of IRE and H-FIRE pulses indicates that a higher-frequency signal content (>100 kHz) may increase our ability to target cells of a higher NCR. Although this analysis offers some insight into the mechanism for cell targeting of H-FIRE, future work in the development of an accurate time-domain model is warranted.

The EphA2 receptor has been identified as overexpressed in various cancers (35–39) in addition to GBM, suggesting a broader application for our results for treatments in other tumor sites for which more traditional surgical or radiotherapy options may be limited, for example, tumors that surround sensitive neural or vascular structures. Areas of increased EphA2 expression are important therapy targets, as elevated EphA2 expression has been correlated with higher pathological grade (40) and poor prognosis (41,42). EphA2 is an important target for this synergistic therapy for another important reason, which is that it may allow for the targeting of highly tumorigenic glioma stem cells, which combinatorial treatments may leave behind due to their highly chemoresistant nature (43). EphA2 receptors have been found to be expressed most highly on tumor-initiating cells, with the highest levels of expression in the most aggressive, stem-cell-like mesenchymal subtype (44). Though the EphA2/ephrinA1 interaction has been the subject of our study, multi-ligand cocktails can also be explored to capitalize on other ephrin interactions in cancer.

The findings presented here highlight the importance of considering the physical phenotypes of cells both for treatment planning and for exploitation to improve treatment efficacy. The classical understanding of electroporation simplifies the relationship between TMP and cell shape and size. However, we have shown that the relationship is more complex, and the vast pulse-frequency parameter space should be further explored to identify novel therapeutic synergies of the sort that we have demonstrated here. Taking into account the complex relationship between these variables may open up the possibility for significantly improved cancer therapies by targeting the physical hallmarks of tumor cells with next-generation combinatorial therapies. Though our findings are presented here in the context of tumor ablation, the importance of considering cellular biophysics extends to other applications of electroporation as well. Applications such as genetic engineering may benefit from manipulating cellular biophysics to more effectively deliver intracellular cargo not only in therapy applications but also as a practice in basic research.

SUPPORTING MATERIAL

Supporting Materials and Methods, one figure, and two tables are available at http://www.biophysj.org/biophysj/supplemental/S0006-3495(17)30664-1.

AUTHOR CONTRIBUTIONS

J.W.I.: study design, cell culture, 3D scaffold construction, confocal microscopy imaging, live-dead staining, mathematical modeling, data analysis and interpretation, and writing of manuscript; E.L.L.: construction of custom electronics, finite-element modeling, data analysis and interpretation, and writing of manuscript; M.L.R.: cell culture, 3D scaffold construction, live-dead staining, and data analysis; G.J.L.: conception of project plan; W.D.: conception of project plan and study design; R.V.D.: conception of project plan, study design, data analysis and interpretation, and writing of manuscript; S.S.V.: conception of project plan, study design, data analysis and interpretation, and writing of manuscript.

ACKNOWLEDGMENTS

We express our gratitude to Daniel Sweeney for useful discussions and assistance in understanding analytical models of electroporation.

This work was supported by the National Cancer Institute of the National Institutes of Health through awards R21CA192042 and R01CA213423, by National Science Foundation CAREER (CBET-1652112) and REU (EEC-1359073) awards, and by a National Cancer Institute Cancer Center Support Grant (award no. P30CA012197) issued to the Wake Forest Baptist Comprehensive Cancer Center.

REFERENCES

1. Weaver, J. C., and Y. A. Chizmadzhev. 1996. Theory of electroporation: a review. *Bioelectrochem. Bioenerg.* 41:135–160.
2. Mir, L. M. 2001. Therapeutic perspectives of in vivo cell electropermeabilization. *Bioelectrochemistry.* 53:1–10.
3. Agerholm-Larsen, B., H. K. Iversen, …, J. Gehl. 2011. Preclinical validation of electrochemotherapy as an effective treatment for brain tumors. *Cancer Res.* 71:3753–3762.
4. Davalos, R. V., I. L. Mir, and B. Rubinsky. 2005. Tissue ablation with irreversible electroporation. *Ann. Biomed. Eng.* 33:223–231.
5. Cannon, R., S. Ellis, …, R. C. Martin, II. 2013. Safety and early efficacy of irreversible electroporation for hepatic tumors in proximity to vital structures. *J. Surg. Oncol.* 107:544–549.
6. Onik, G., and B. Rubinsky. 2010. Irreversible electroporation: first patient experience focal therapy of prostate cancer. *In* Irreversible Electroporation. B. Rubinsky, editor. Springer, pp. 235–247.
7. Martin, R. C., 2nd, D. Kwon, …, K. Watkins. 2015. Treatment of 200 locally advanced (stage III) pancreatic adenocarcinoma patients with irreversible electroporation: safety and efficacy. *Ann. Surg.* 262:486–494, discussion 492–494.
8. Neal, R. E., 2nd, J. L. Millar, …, K. R. Thomson. 2014. In vivo characterization and numerical simulation of prostate properties for non-thermal irreversible electroporation ablation. *Prostate.* 74:458–468.
9. Lee, E. W., C. Chen, …, S. T. Kee. 2010. Advanced hepatic ablation technique for creating complete cell death: irreversible electroporation. *Radiology.* 255:426–433.
10. Guo, Y., Y. Zhang, …, A. C. Larson. 2010. Irreversible electroporation therapy in the liver: longitudinal efficacy studies in a rat model of hepatocellular carcinoma. *Cancer Res.* 70:1555–1563.
11. Daniels, C., and B. Rubinsky. 2009. Electrical field and temperature model of nonthermal irreversible electroporation in heterogeneous tissues. *J. Biomech. Eng.* 131:071006.
12. Lee, E. W., C. T. Loh, and S. T. Kee. 2007. Imaging guided percutaneous irreversible electroporation: ultrasound and immunohistological correlation. *Technol. Cancer Res. Treat.* 6:287–294.
13. Bonakdar, M., E. L. Latouche, …, R. V. Davalos. 2015. The feasibility of a smart surgical probe for verification of ire treatments using electrical impedance spectroscopy. *IEEE Trans. Biomed. Eng.* 62:2674–2684.
14. Neal, R. E., II, J. H. Rossmeisl, Jr., …, R. V. Davalos. 2014. In vitro and numerical support for combinatorial irreversible electroporation and electrochemotherapy glioma treatment. *Ann. Biomed. Eng.* 42: 475–487.
15. Wykosky, J., D. M. Gibo, …, W. Debinski. 2005. EphA2 as a novel molecular marker and target in glioblastoma multiforme. *Mol. Cancer Res.* 3:541–551.
16. Hatano, M., J. Eguchi, …, H. Okada. 2005. EphA2 as a glioma-associated antigen: a novel target for glioma vaccines. *Neoplasia.* 7:717–722.
17. Liu, D.-P., Y. Wang, …, D. Xie. 2007. Ephrin-A1 is a negative regulator in glioma through down-regulation of EphA2 and FAK. *Int. J. Oncol.* 30:865–871.
18. Wykosky, J., E. Palma, …, W. Debinski. 2008. Soluble monomeric EphrinA1 is released from tumor cells and is a functional ligand for the EphA2 receptor. *Oncogene.* 27:7260–7273.
19. Wykosky, J., D. M. Gibo, and W. Debinski. 2007. A novel, potent, and specific ephrinA1-based cytotoxin against EphA2 receptor expressing tumor cells. *Mol. Cancer Ther.* 6:3208–3218.
20. Ferluga, S., R. Hantgan, …, W. Debinski. 2013. Biological and structural characterization of glycosylation on ephrin-A1, a preferred ligand for EphA2 receptor tyrosine kinase. *J. Biol. Chem.* 288:18448–18457.
21. Miao, H., E. Burnett, …, B. Wang. 2000. Activation of EphA2 kinase suppresses integrin function and causes focal-adhesion-kinase dephosphorylation. *Nat. Cell Biol.* 2:62–69.
22. Eppich, H. M., R. Foxall, …, D. T. Scadden. 2000. Pulsed electric fields for selection of hematopoietic cells and depletion of tumor cell contaminants. *Nat. Biotechnol.* 18:882–887.
23. Agarwal, A., I. Zudans, …, S. G. Weber. 2007. Effect of cell size and shape on single-cell electroporation. *Anal. Chem.* 79:3589–3596.
24. van den Bos, W., D. M. de Bruin, …, J. J. de la Rosette. 2014. The safety and efficacy of irreversible electroporation for the ablation of prostate cancer: a multicentre prospective human in vivo pilot study protocol. *BMJ Open.* 4:e006382.
25. Ivey, J. W., E. L. Latouche, …, S. S. Verbridge. 2015. Targeted cellular ablation based on the morphology of malignant cells. *Sci. Rep.* 5: 17157.
26. Arena, C. B., M. B. Sano, …, R. V. Davalos. 2011. High-frequency irreversible electroporation (H-FIRE) for non-thermal ablation without muscle contraction. *Biomed. Eng. Online.* 10:102.
27. Foster, K. R. 2000. Thermal and nonthermal mechanisms of interaction of radio-frequency energy with biological systems. *IEEE Trans. Plasma Sci.* 28:15–23.
28. Arena, C. B., M. B. Sano, …, R. V. Davalos. 2011. Theoretical considerations of tissue electroporation with high-frequency bipolar pulses. *Ieee T Bio-Med Eng.* 58:1474–1482.
29. Cross, V. L., Y. Zheng, …, A. D. Stroock. 2010. Dense type I collagen matrices that support cellular remodeling and microfabrication for studies of tumor angiogenesis and vasculogenesis in vitro. *Biomaterials.* 31:8596–8607.
30. Sano, M. B., C. B. Arena, …, R. V. Davalos. 2014. In-vitro bipolar nano- and microsecond electro-pulse bursts for irreversible electroporation therapies. *Bioelectrochemistry.* 100:69–79.
31. Bhonsle, S. P., C. B. Arena, …, R. V. Davalos. 2015. Mitigation of impedance changes due to electroporation therapy using bursts of high-frequency bipolar pulses. *Biomed. Eng. Online.* 14 (*Suppl 3*):S3.
32. White, F. H., and K. Gohari. 1981. Variations in the nuclear-cytoplasmic ration during epithelial differentiation in experimental oral carcinogenesis. *J. Oral Pathol.* 10:164–172.

33. Jin, Y., L. J. Yang, and F. H. White. 1995. Preliminary assessment of the epithelial nuclear-cytoplasmic ratio and nuclear volume density in human palatal lesions. *J. Oral Pathol. Med.* 24:261–265.

34. Boyd, A. W., P. F. Bartlett, and M. Lackmann. 2014. Therapeutic targeting of EPH receptors and their ligands. *Nat. Rev. Drug Discov.* 13:39–62.

35. Pasquale, E. B. 2010. Eph receptors and ephrins in cancer: bidirectional signalling and beyond. *Nat. Rev. Cancer.* 10:165–180.

36. Miao, H., and B. Wang. 2012. EphA receptor signaling—complexity and emerging themes. *Semin. Cell Dev. Biol.* 23:16–25.

37. Zelinski, D. P., N. D. Zantek, …, M. S. Kinch. 2001. EphA2 overexpression causes tumorigenesis of mammary epithelial cells. *Cancer Res.* 61:2301–2306.

38. Miyazaki, T., H. Kato, …, H. Kuwano. 2003. EphA2 overexpression correlates with poor prognosis in esophageal squamous cell carcinoma. *Int. J. Cancer.* 103:657–663.

39. Thaker, P. H., M. Deavers, …, A. K. Sood. 2004. EphA2 expression is associated with aggressive features in ovarian carcinoma. *Clin. Cancer Res.* 10:5145–5150.

40. Li, X., Y. Wang, …, X. Zhang. 2007. Expression of EphA2 in human astrocytic tumors: correlation with pathologic grade, proliferation and apoptosis. *Tumour Biol.* 28:165–172.

41. Wang, L.-F., E. Fokas, …, H.-X. An. 2008. Increased expression of EphA2 correlates with adverse outcome in primary and recurrent glioblastoma multiforme patients. *Oncol. Rep.* 19:151–156.

42. Liu, F., P. J. Park, …, M. D. Johnson. 2006. A genome-wide screen reveals functional gene clusters in the cancer genome and identifies EphA2 as a mitogen in glioblastoma. *Cancer Res.* 66:10815–10823.

43. Liu, G., X. Yuan, …, J. S. Yu. 2006. Analysis of gene expression and chemoresistance of CD133+ cancer stem cells in glioblastoma. *Mol. Cancer.* 5:67.

44. Binda, E., A. Visioli, …, A. L. Vescovi. 2012. The EphA2 receptor drives self-renewal and tumorigenicity in stem-like tumor-propagating cells from human glioblastomas. *Cancer Cell.* 22:765–780.

Biophysical Journal, Volume *113*

Supplemental Information

Enhancing Irreversible Electroporation by Manipulating Cellular Biophysics with a Molecular Adjuvant

Jill W. Ivey, Eduardo L. Latouche, Megan L. Richards, Glenn J. Lesser, Waldemar Debinski, Rafael V. Davalos, and Scott S. Verbridge

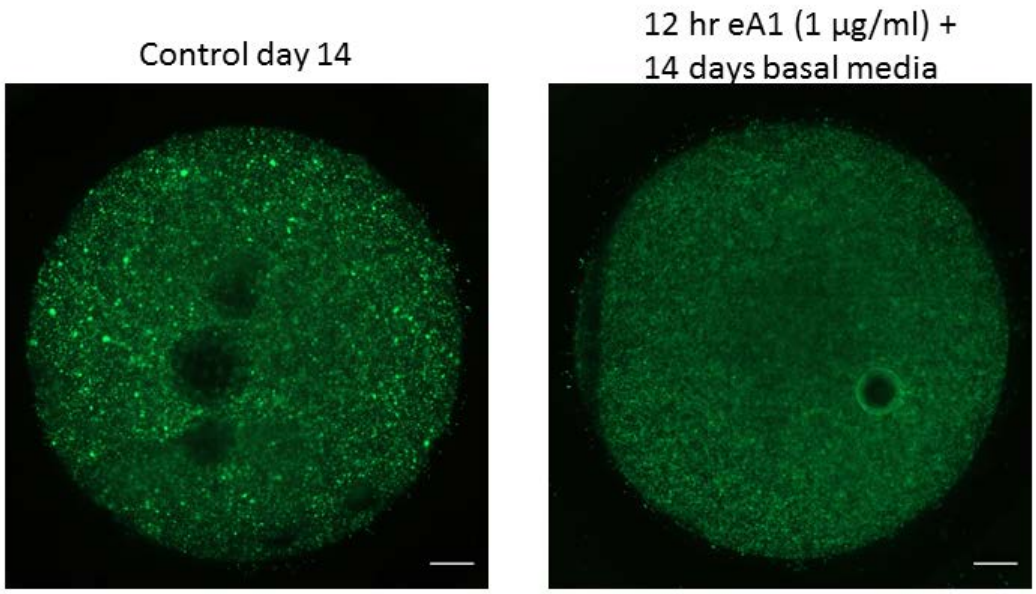

Figure S1. Live dead staining of cells cultured with eA1 in hydrogels*. Cells were cultured in collagen hydrogels with 1 µg/ml eA1 media for 12 h, which was then replaced with basal media and cells were cultured out to 14 days. Calcien AM staining of the live cells (green) and ethD-III staining of dead cells (red) shows no visible cell death for eA1 treatment. Scale bar 1 mm.*

Table S1: *Physical properties used in finite element models of hydrogel treatments. * measured values, ‡ default material values in COMSOL*

Parameter	Symbol	Value	Unit	Reference
IRE Voltage	V_{IRE}	450	[V]	*
H-FIRE Voltage	V_{HFIRE}	450-700	[V]	*
Electrode Density	ρ_e	7850	[kg/m^3]	‡
Electrode Specific Heat Capacity	Cp_e	475	[J/(kg·K)]	‡
Electrode Thermal Conductivity	k_e	44.5	[W/(m·K)]	‡
Electrode Conductivity	σ_e	4.03x10^6	[S/m]	‡
Electrode Permittivity	ε_e	1		‡
Hydrogel Density	ρ_h	997.8	[kg/m^3]	(45)
Hydrogel Specific Heat Capacity	Cp_h	4181.8	[J/(kg·K)]	(45)
Hydrogel Thermal Conductivity	k_h	0.6	[W/(m·K)]	(45)
Hydrogel Conductivity	σ_h	1.2	[S/m]	(45)
Hydrogel Permittivity	ε_h	0		(45)

Table S2: *Physical properties used in finite element models of single cells. * measured values, ‡ approximation based on water composition*

Parameter	Symbol	Value	Units	Reference
Media Conductivity	σ_m	0.98	[S/m]	*
Media Permittivity	ε_m	$80\varepsilon_0$	[F/m]	‡
Cytoplasm Conductivity	σ_{cyt}	0.3	[S/m]	(46)
Cytoplasm Permittivity	ε_{cyt}	$154.4\varepsilon_0$	[F/m]	(47)
Nucleoplasm Conductivity	σ_{nuc}	1.35	[S/m]	(46)
Nucleoplasm Permittivity	ε_{nuc}	$52\varepsilon_0$	[F/m]	(46)
Cell Membrane Thickness	t_{mem}	$5x10^{-9}$	[m]	(48)
Nuclear Membrane Thickness	t_{Nmem}	$40x10^{-9}$	[m]	(46)
Cell Membrane Conductivity	σ_{mem}	$3x10^{-7}$	[S/m]	(49)
Cell Membrane Permittivity	ε_{mem}	$8.57\varepsilon_0$	[F/m]	(50)
Nuclear Membrane Conductivity	σ_{Nmem}	$6x10^{-3}$	[S/m]	(46)
Nuclear Membrane Permittivity	ε_{Nmem}	$28\varepsilon_0$	[F/m]	(46)
Domain Side Length	L_d	$300x10^{-6}$	[m]	-
Benign Cell Radius	R_c	$20x10^{-6}$	[m]	*
Benign Nuclear Radius	R_n	$6.2x10^{-6}$	[m]	*
Malignant Cell Radius	R_{mc}	$20x10^{-6}$	[m]	*
Malignant Nuclear Radius	R_{mn}	$14.7x10^{-6}$	[m]	*
Malignant Cell Radius (post-ephrin)	R_{mce}	$16.7x10^{-6}$	[m]	*
Malignant Nuclear Radius (post-ephrin)	R_{mne}	$14.7x10^{-6}$	[m]	*

References

45. Rubinsky, B. 2007. Irreversible electroporation in medicine. Technology in cancer research & treatment 6:255-259.
46. Asami, K., Y. Takahashi, and S. Takashima. 1989. Dielectric-Properties of Mouse Lymphocytes and Erythrocytes. Biochim Biophys Acta 1010:49-55.
47. Yang, J., Y. Huang, X. J. Wang, X. B. Wang, F. F. Becker, and P. R. C. Gascoyne. 1999. Dielectric properties of human leukocyte subpopulations determined by electrorotation as a cell separation criterion. Biophysical Journal 76:3307-3314.
48. Gascoyne, P. R. C., R. Pethig, J. P. H. Burt, and F. F. Becker. 1993. Membrane-Changes Accompanying the Induced-Differentiation of Friend Murine Erythroleukemia-Cells Studied by Dielectrophoresis. Biochim Biophys Acta 1149:119-126.
49. Sano, M. B., E. A. Henslee, E. M. Schmelz, and R. V. Davalos. 2011. Contactless dielectrophoretic spectroscopy: Examination of the dielectric properties of cells found in blood. Electrophoresis 32:3164-3171.
50. Alberts, B., D. Bray, J. Lewis, M. Raff, K. Roberts, J. D. Watson, and A. Grimstone. 1995. Molecular Biology of the Cell (3rd edn). Trends in Biochemical Sciences 20:210-210.
51. Huang, S.-H., L.-Y. Hung, and G.-B. Lee. 2016. Continuous nucleus extraction by optically-induced cell lysis on a batch-type microfluidic platform. Lab on a Chip 16:1447-1456.